DOI: https://doi.org/10.62985/j.huit_ojs.vol26.no2E.402

# ADAPTIVE VIRTUAL SYNCHRONOUS MACHINE PARAMETER TUNING FOR REGFM-B1 GRID-FORMING INVERTERS UNDER CURRENT SATURATION CONSTRAINTS

**Pham Hong Thanh[1], Le Van Dai[2,*]**

[1]*Thu Dau Mot University*

[2]*Electric Power System Research Group,*

*Industrial University of Ho Chi Minh City*, *Vietnam*

*Email: *levandai@iuh.edu.vn*

Received: 10 January 2026; Revised: 15 March 2026; Accepted: 8 April 2026

## ABSTRACT

The increasing penetration of inverter-based resources has significantly reduced effective system inertia, posing serious challenges to frequency stability in weak power systems. While virtual synchronous machine (VSM) control provides synthetic inertia, conventional fixed-parameter designs suffer from an inherent trade-off between frequency nadir and transient settling speed. Furthermore, many optimization-based tuning methods disregard the non-linear operational limits of power semiconductors, leading to non-smooth search spaces and sub-optimal local equilibria. This paper proposes a hardware-constrained adaptive VSM control framework compliant with the reference explicit grid-forming model B1 (REGFM-B1) standard, in which virtual inertia and damping parameters are optimized using a particle swarm optimization (PSO) algorithm with a time-varying inertia weight (TVIW) strategy. The inertia weight is gradually reduced from 0.9 to 0.4, enabling effective global exploration despite saturation-induced discontinuities while ensuring accurate local convergence. Nonlinear current-limiting constraints are explicitly embedded into the optimization process to guarantee physically realizable solutions. The proposed method is validated through MATLAB simulations on a 10 MVA grid-forming battery energy storage system under ten disturbance scenarios with short-circuit ratios ranging from 1.5 to 3.0. Results show a 98.1% improvement in frequency nadir and a 60.0% reduction in settling time compared with fixed-parameter benchmarks. Moreover, the proposed strategy achieved an average ITAE reduction of 7.52% relative to standard PSO and 6.44% compared to modern adaptive PSO (APSO) variants, while strictly maintaining a 1.2 pu current limit.

*Keywords:* Virtual synchronous machine, grid-forming inverter, REGFM-B1, time-varying Inertia weight, particle swarm optimization, current saturation, weak power system.

## 1. INTRODUCTION

The global push for decarbonization is fundamentally transforming power systems by replacing synchronous machines with inverter-based resources (IBRs) [1]. As traditional generation is displaced, modern grids exhibit a significant reduction in system inertia and short-circuit strength thereby weakening synchronizing torque and frequency self-regulation capability. Unlike synchronous generators, standard IBRs utilizing phase-locked loops (PLL) decouple the renewable energy source from grid frequency dynamics, preventing direct inertial response and thereby creating severe stability vulnerabilities [1]. The North American Electric Reliability Corporation (NERC) has documented these risks, noting that high-IBR systems are prone to medium-frequency

oscillations (MFO) and transient instability following islanding events. Similarly, recent studies in Vietnam have confirmed that the increasing penetration of renewable energy sources (RES) poses tangible threats to operational security, particularly under weak-grid conditions characterized by low SCR and limited fault current contribution [2]. Furthermore, modern grid codes, such as the IEEE P2800 standard, have established stringent performance requirements for inverter-based resources, particularly regarding frequency nadir and settling time behavior during transient events, which are explicitly defined as performance-critical metrics for inverter-based resources [3, 4].

To address these challenges, virtual synchronous machine (VSM) control has emerged as a promising solution [2]. By emulating the swing equation dynamics of classical machines, VSMs endow IBRs with grid-forming (GFM) capabilities and synthetic inertia support, thereby enabling frequency-setting operation without relying on a phase-locked loop [5]. This methodology enables seamless integration of IBR synchronous operation even at high renewable penetration levels [6, 7]. While numerous studies have demonstrated the superiority of VSMs over conventional grid-following controls, most existing approaches rely on fixed virtual inertia and damping parameters. These fixed settings are typically tuned for nominal conditions and fail to adapt to rapid topology changes or weak grid characteristics, resulting in sub-optimal trade-offs between inertial support and transient recovery speed [8]. Consequently, there is a critical need for adaptive control strategies that leverage optimization algorithms to tune parameters in real-time. Recent studies have explored adaptive tuning of VSG parameters using reinforcement learning techniques, such as Soft Actor-Critic, to enhance stability under varying grid conditions [9]. However, their practical deployment is often hindered by high computational burden and the lack of explicit consideration of instantaneous semiconductor current limits.

However, significant research gaps persist in translating academic VSM models for practical deployment. The majority of current research utilizes simplified average models that disregard the nonlinear current-limiting capabilities of power semiconductors. In reality, injecting high virtual inertia during faults can cause the inverter output current to spike, triggering immediate protection trips and resulting in unit loss. Furthermore, the lack of standardization in academic models hinders industrial adoption. The reference explicit GFM model B1 (REGFM-B1) model, recently approved by WECC and NERC, offers a standardized framework that explicitly accounts for two-stage priority current limiting, yet it has rarely been explored in the context of adaptive optimization [10]. Unlike conventional tuning methods, the explicit incorporation of nonlinear current-limiting constraints into the REGFM-B1 model results in a highly non-convex and discontinuous objective function landscape, which often leads standard metaheuristic algorithms to settle in sub-optimal local equilibria, particularly in regions where current saturation activates and the objective gradient becomes ill-defined.

This work develops a new adaptive VSM control system based on the REGFM-B1 algorithm, accounting for nonlinear current limitations, by implementing our time-varying inertia weight particle swarm optimization (TVIW-PSO) approach to find solutions beyond local optima and to better explore and exploit the problem space. Our method accurately adjusts inertia, damping, and gains, providing an example of a system that will exhibit superior dynamic performance while remaining able to satisfy the current limits.

To bridge the gap between theoretical VSM models and practical hardware limitations, this paper proposes a unified constraint-aware control framework for REGFM-B1 inverters, distinct from prior works that treat controller tuning and protection in isolation. The primary contribution of this work lies in formulating a safety-critical tuning problem that explicitly incorporates nonlinear priority-current-limited constraints, ensuring that the optimized inertia response remains within safe operating limits during severe voltage dips. Furthermore, we introduce an adaptive-protection co-design mechanism that dynamically bounds the virtual inertia trajectory by the instantaneous current margin to prevent integrator windup. To evaluate the effectiveness of the proposed TVIW-PSO, a comprehensive benchmarking study is conducted, comparing its

performance against Standard PSO and modern Adaptive PSO (APSO) variants [9-11] designed for power system stability. While techniques such as APSO [9, 11] improve exploration in distribution systems, they struggle to navigate the highly nonconvex, discontinuous search space induced by the nonlinear current-limiting constraints of the REGFM-B1 model. Our proposed TVIW-PSO addresses these limitations by using a quadratic inertia-weight decay strategy, enabling the particles to escape suboptimal local equilibria where standard adaptive variants often stagnate.

## 2. SYSTEM MODELING AND PROPOSED CONTROL FRAMEWORK

Ensuring grid stability under high renewable penetration requires robust modeling frameworks that bridge theoretical concepts with practical implementation. This section presents a comprehensive framework that combines VSM dynamics, adaptive control laws, and semiconductor constraints, based on the REGFM-B1 standard. Electrical ratings and system parameters are provided in physical units, while all control variables and dynamic state variables are expressed in the per-unit (pu) system unless otherwise specified.

### 2.1. Grid-Forming Inverter Architecture

Prior studies have established that VSM control enables inverter-based resources to operate in GFM mode by emulating synchronous machine dynamics. However, existing fixed-parameter models exhibited trade-offs between frequency support and settling behaviour across all designs, reflecting the inherent coupling between virtual inertia magnitude and transient damping performance. Therefore, a new model development approach was established that included adaptive inertia adjustment and the explicit representation of semiconductor protection constraints, which are critical for ensuring stable operation during large-signal disturbances.

The reference explicit grid-forming model B1 (REGFM-B1), endorsed by WECC and referenced by NERC, served as the architectural basis for this modelling framework, providing relevance to industry and ensuring compliance with grid code requirements, thereby ensuring compatibility with emerging industry-standard grid-forming specifications [8]. This framework extends prior academic models, which generally did not incorporate converter-level protection, by including an inner current control loop, an active power-frequency ($P$–$\omega$) control model, and a reactive power-voltage ($Q$–$V$) control model. The 10 MVA/ 22 kV GFM BESS is modeled as connected to a weak grid with a short-circuit ratio (SCR) below 3.0, a regime known to amplify control-grid interactions and reduce voltage stiffness. The connection is established via a transmission line represented by a Thévenin equivalent impedance $Z_g = R_g + jL_g$. This impedance is specifically configured with high values to simulate severe voltage coupling challenges, as identified in [12]. Semiconductor protection against overcurrent is provided by limiting the output current to a ceiling of 1.2 pu, a typical thermal limit in industrial applications, beyond which semiconductor junction temperatures and device lifetime may be severely compromised.

Figure 1 illustrates the proposed system architecture, consisting of the power stage and the VSM control block, highlighting the hierarchical separation between control functions and hardware protection mechanisms. The power stage includes a DC energy source implemented as a battery energy storage system (BESS), a three-phase voltage-source inverter (VSI) with insulated-gate bipolar transistor (IGBT) switches, a passive LCL output filter, and the grid connection impedance, denoted $Z_g$ [10]. The VSM control block uses frequency deviation and active power measurements from the power detector block, which are retrieved from the voltage and current sampled at the inverter terminals. The control references $P_{ref}$ and $Q_{ref}$ were provided by higher-level dispatch logic. The priority current limiting block was placed below the control block to prevent semiconductor devices from excessive current by enforcing a 1.2 pu current limit. This hierarchical placement ensures that hardware protection acts as a hard constraint on the outer

adaptive control, thereby preventing integrator windup and unsafe control actions during large-signal disturbances.

In a manner that simulates the swing equation and damping behavior of a conventional synchronous machine, the VSM controller enables static inverters to contribute virtual inertia and damping in a fully GFM manner, independent of external phase-locked loops [6].

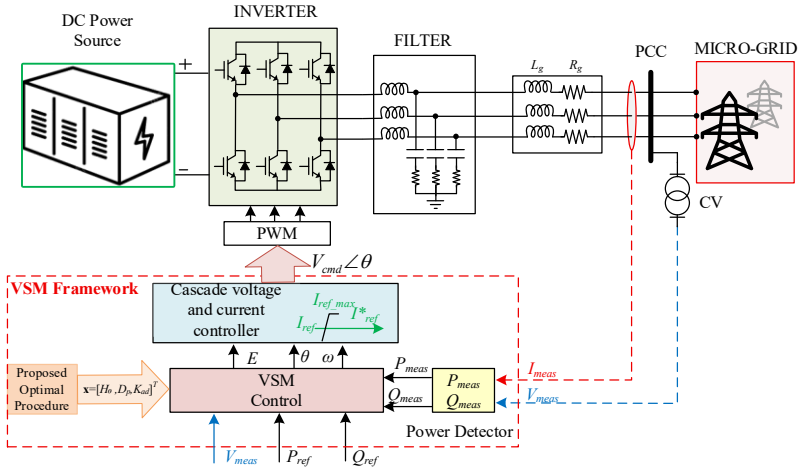


*Fig. 1.* Schematic diagram of the GFM BESS system based on the REGFM-B1 architecture connected to a weak grid.

## 2.2. Virtual Synchronous Machine Dynamics

The control architecture is decomposed into two primary control loops: the $P$–$\omega$ loop governing frequency regulation, and the $Q$–$V$ loop managing voltage support. This separation had been justified in prior work by the inherent weak coupling between the dynamics of active and reactive power in grid operation.

The classical swing equation described the frequency dynamics in (1), which had previously been adapted for inverter control by Zhong and Weiss [1]:

$$\begin{cases} 2H\dfrac{d\omega}{dt} = P_m - P_e - D_p.\Delta\omega \\ \dfrac{d\theta}{dt} = \Delta\omega.\omega_n \end{cases} \tag{1}$$

where $\Delta\omega$ denotes the frequency deviation (pu); $\theta$ is the voltage phase angle (rad), and $\omega_n$ is the nominal angular frequency (rad/s). $P_m$ and $P_e$ are the virtual mechanical input power and electrical output power (pu), respectively. $H$ is the virtual inertia constant (s), defined as the ratio of stored energy to rated power; $D_p$ is a dimensionless damping coefficient, and $d\Delta\omega/dt$ represents the RoCoF (pu/s). However, this comes at the cost of prolonging the settling transient, which creates an asymmetry. A similar correlation exists between higher damping and suppressed oscillations, while the response time to small disturbances may be longer. This trade-off has previously been demonstrated to involve difficulties associated with weak networks due to changes in network topology and unsymmetrical line impedances. Therefore, fixing parameters will not ensure optimal operation performance across multiple operating conditions.

Voltage regulation at the point of common coupling (PCC) was achieved through reactive power and voltage-error feedback. The virtual exciter in (2) is modelled as a first-order lag:

$$\frac{dE}{dt} = \frac{1}{T_v}\left[\, k_q\,(Q_{ref} - Q_e) + (V_{ref} - V_{meas}) - E \,\right] \tag{2}$$

where $E$ is the internal voltage magnitude of the VSG (pu), representing the internal electromotive force behind the virtual impedance; $T_v$ is the virtual excitation time constant (s); $k_q$ is the reactive power droop gain. $Q_{ref}$ and $Q_e$ are the reference and measured reactive power (pu), respectively, while $V_{ref}$ and $V_{meas}$ are the reference and measured PCC voltage magnitudes (pu). The term $\frac{dE}{dt}$ represents the rate of change of the internal voltage (pu/s).

Physically, $T_v$ captures the electromagnetic transient associated with the field winding in a synchronous machine, thereby emulating the excitation system dynamics. The term $k_q(Q_{ref} - Q_e)$ provides reactive power droop control, whereas $(V_{ref} - V_{meas})$ introduces voltage error feedback. In accordance with REGFM-B1 specifications [8], $T_v$ is selected to ensure a clear separation between the voltage loop bandwidth and the faster inner current control loop, thereby enhancing stability during transient voltage recovery.

The internal EMF magnitude $E$ determined the amplitude of the voltage the PWM modulator would synthesize at the inverter terminals. Because $E$ originated internally rather than from the grid voltage signal, the inverter could maintain grid-forming behaviour, even during voltage collapse or islanding scenarios, which is different from grid-following inverters [7].

### 2.3. Adaptive Control Strategy and Hardware Constraints

To mitigate the trade-offs inherent in fixed-parameter designs, a real-time adaptive control law is established. Building on the adaptive concept in [10], but departing from their threshold-based bang-bang approach, we propose a continuous linear modulation strategy. This formulation establishes a direct proportional relationship between instantaneous frequency deviation and virtual inertia to prevent control chattering, defined as follows (3):

$$H(t) = \min(H_0 + K_{ad} \left|\Delta\omega(t)\right|, H_{\max}) \tag{3}$$

where $H(t)$ is the adaptive virtual inertia constant (s), $H_0$ is the baseline inertia (s), $K_{ad}$ is the adaptive inertia gain (s/pu), $\Delta\omega(t)$ is the instantaneous frequency deviation (pu), and $H_{max}$ is the upper bound of the inertia constant (s).

It is observed that severe electrical faults cause large frequency swings exceeding 0.3 Hz during significant voltage dips. Because of this, a significant level of inertial support is required to limit the magnitudes of nadir and RoCoF. In comparison, small load disturbances result in low-frequency deviations of less than 0.1 Hz. Thus, the use of higher inertia in these cases would reduce settling performance. The linear gain structure $K_{ad}$ in equation (3) allowed for the automatic differentiation between fault-induced and operational transients [10]. As analyzed in [13], excessive inertia in weak grids can lead to oscillatory instability. Therefore, a saturation limit is essential. In this study, we empirically selected $H_{max} = 1.5H_0$ to balance between transient support and stability recovery.

The damping coefficient $D_p$ for the adaptive control law was calculated using the IPSO algorithm, which is illustrated in Section 3, and remains constant during real-time operation. This approach reflects the understanding that damping primarily acts to absorb oscillatory energy, and its optimal value does not significantly depend on instantaneous grid conditions.

The nonlinear current limiting constraint was formulated as (4):

$$I_{ref}^{*} = \begin{cases} I_{ref} & \text{if } |I_{ref}| \le I_{max} \\ \dfrac{I_{max}}{|I_{ref}|} \cdot I_{ref} & \text{if } |I_{ref}| > I_{max} \end{cases} \tag{4}$$

where $I_{ref}$ is the reference current vector (pu), $I_{ref}^{*}$ is the limited current reference (pu), and $I_{max}$ is the maximum allowable current magnitude (pu). This formulation preserves the current angle

while limiting its magnitude. Typically, $I_{max}$ is set to 1.2 pu based on the REGFM-B1 standard and thermal limits [14]. This magnitude clipping preserved the current phase angle, thus maintaining inner-loop stability. The nonlinearity introduced by saturation activation had been shown to cause integrator windup in conventional PI regulators if control gains were not explicitly optimized under saturated conditions. The necessity of accounting for this constraint during parameter optimization had justified the selection of PSO over traditional linear tuning methods.

### 2.4. Test Environment Definition

Robustness validation is conducted against 10 distinct disturbance scenarios, ranging from minor load transitions to critical cascading faults. Grid conditions were established so that SCR values ranged from 1.5 to 3.0, encompassing extreme weak-grid conditions representative of remote renewable injection points. The scenario suite was deliberately designed to activate the current-limiting saturation nonlinearity, thereby ensuring that the optimized parameters would be valid under both linear and nonlinear operating regimes.

## 3. THE PROPOSED OPTIMIZATION ALGORITHM

Conventional parameter tuning techniques - such as pole-placement methods, Ziegler-Nichols rules, or manual iteration - often prove ineffective for this multi-objective, nonconvex optimization problem. The discontinuity introduced by the current saturation constraint in (4) generates multiple local minima within the cost landscape, causing gradient-based methods and fixed-inertia PSO algorithms to suffer from premature convergence. To address these limitations, this study employs an improved PSO with adaptive inertia weight decay.

### 3.1. Optimization Problem Formulation

The cost function is selected to penalize frequency deviations, with explicit emphasis on suppressing late-transient oscillations. The integral of time-weighted absolute error (ITAE) was chosen by (5):

$$J_{cost} = \int_0^{T_{sim}} t. |\Delta\omega(t)| dt + \Psi_{penalty} \tag{5}$$

where $t$ is time (s), $\Delta\omega(t)$ is the frequency deviation (pu), and $\Psi_{penalty}$ is a dimensionless penalty term. The resulting cost $J_{cost}$ is a performance index based on time-weighted frequency deviation. Specifically, this term is configured to impose a weighted penalty of 10 on frequency overshoot beyond the operational band of ±0.01 pu and strictly applies a discrete instability cost of $10^4$ if the deviation exceeds the critical 0.05 pu threshold. This time-weighted objective favors rapid settling over mere peak error minimization. The optimization searches (6) for the optimal decision vector $x$:

$$x = \left[ H_0,\ D_p,\ K_{ad} \right]^T \tag{6}$$

where $H_0$ is expressed in seconds (s), $D_p$ is a dimensionless damping coefficient, and $K_{ad}$ is the adaptive inertia gain (s/pu). The search ranges are defined as $H_0 \in [0.1, 10]$ s, $D_p \in [10, 500]$, and $K_{ad} \in [0, 100]$ s/pu. The lower bound on $H_0$ reflected the observation that excessively low inertia causes the system to behave as a near-current source, losing the synchronizing advantages sought by VSM design. Concerns about noise amplification constrained the upper bound on $D_p$.

To ensure the robustness of the derived parameters, a worst-case design strategy is adopted. Instead of optimizing for benign conditions, the algorithm was trained on the most critical disturbance scenario.

### 3.2. Particle Swarm Optimization with Time-Varying Inertia Weight

PSO is selected for its ability to explore nonconvex landscapes without gradient information. Particle $i$ at iteration $k$ updated its velocity and position as (7) and (8):

$$v_i^{k+1} = w \cdot v_i^k + c_1 r_1 (P_{best,i}^k - x_i^k) + c_2 r_2 (G_{best}^k - x_i^k) \tag{7}$$

$$x_i^{k+1} = x_i^k + v_i^{k+1} \tag{8}$$

where $P_{best,i}$ and $G_{best}$ denote personal and global best solutions, $r_1$ and $r_2$ are uniform random numbers in (0, 1), and $c_1 = c_2 = 2.0$. The decision vector $x_i$ contains parameters with different physical dimensions; therefore, normalization is implicitly handled within the optimization process to ensure numerical stability.

Standard PSO uses a constant inertia $w \approx 0.7$, which often leads to premature convergence. Here, a quadratic decay schedule is adopted by (9):

$$w(k) = w_{max} - (w_{max} - w_{min}).(k / k_{max})^2 \tag{9}$$

where $w(k)$ is the inertia weight at iteration $k$ (dimensionless), $w_{max}$ and $w_{min}$ are the maximum and minimum inertia weights, respectively, $k$ is the current iteration index, and $k_{max}$ is the maximum number of iterations.

The specific configuration of the TVIW-PSO algorithm, including the upper and lower bounds of the inertia weight and the acceleration coefficients, is detailed in Table 1. By employing the quadratic decay schedule in (9), the inertia weight decreases smoothly from a high initial value to a lower final value. During the early stages of the optimization process, a larger inertia weight promotes global exploration, enabling particles to escape local optima induced by saturation-related discontinuities. As the iteration progresses, the inertia weight decreases, enhancing local exploitation and ensuring convergence toward the global optimum. Regarding implementation, the TVIW-PSO algorithm is utilized for offline parameter optimization during the design phase. Once the optimal gains are determined, the real-time control law $H = H_0 + K_{ad} |\Delta\omega|$ is a simple linear function that imposes negligible computational overhead on the inverter's digital signal processor (DSP) compared to standard fixed-parameter VSMs [9, 10].

*Table 1.* Optimization algorithm configurations for benchmarking

| Parameter | Symbol | Description |
|---|---|---|
| Population size | 40 | Number of particles |
| Maximum iterations | 50 | Termination criterion ($k_{max}$) |
| Inertia weight (TVIW) | 0.9 to 0.4 | Proposed quadratic decay strategy |
| APSO Strategy | Adaptive | Evolutionary state-based adaptation [11] |
| Acceleration coefficients | $c_1 = 2.0$, $c_2 = 2.0$ | Social/cognitive balance |
| Search range ($H_0$) | [0.1, 10] s | Baseline inertia bounds |
| Search range ($D_p$) | [10, 500] | Damping coefficient bounds |
| Search range ($K_{ad}$) | [0, 100] s/pu | Adaptive gain bounds |
| Simulation duration | 5 s | Time-domain horizon |

### 3.3. Algorithm Procedure

The optimization is implemented in MATLAB. A swarm of 40 particles is initialized with random $H_0$, $D_p$ and $K_{ad}$ within the prescribed bounds. For each particle and each iteration, a 5-s

time-domain simulation of the REGFM-B1 system is run under one of the ten disturbance scenarios. The ITAE cost is computed from the resulting frequency trajectory; $P_{best}$ and $G_{best}$ were updated whenever an improvement occurred. Particle velocities are then recomputed according to (7)-(9), and positions are updated using (8), with boundary clamping enforcing feasible parameter values. This process is repeated for 50 iterations until convergence, as shown in the flowchart in Fig. 2.

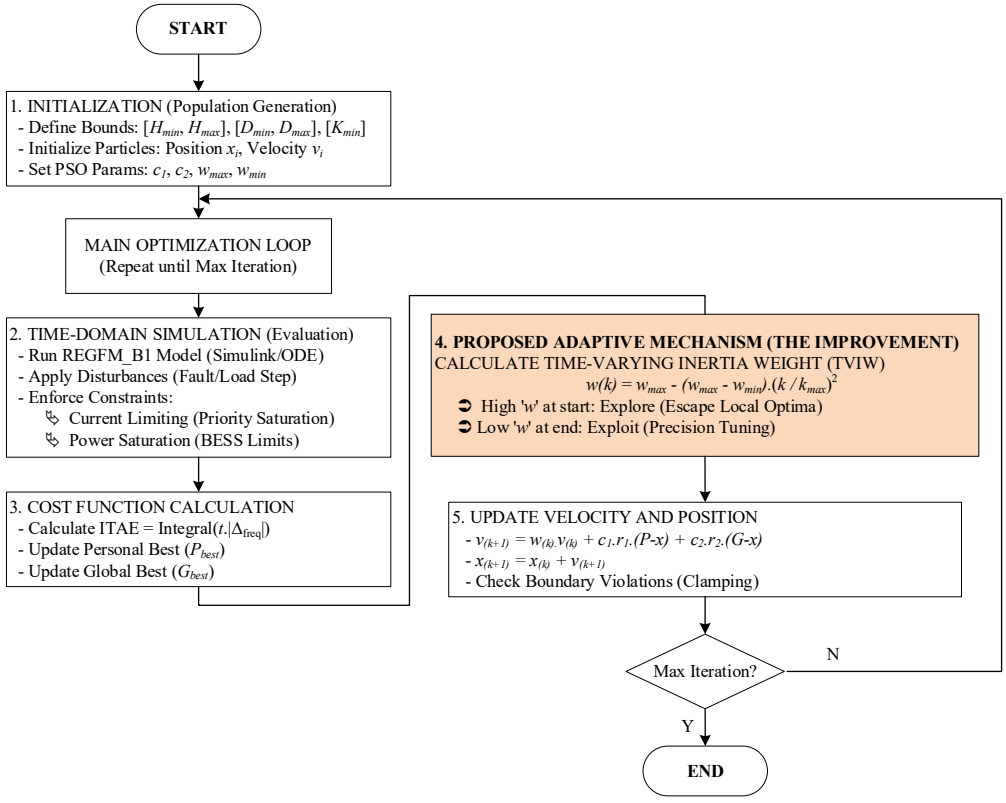


*Fig. 2.* Flowchart of the proposed TVIW-PSO algorithm for optimal VSM parameter tuning.

### 3.4. Simulation Parametrization

The plant model represents a 10 MVA/ 22 kV grid-forming inverter-storage unit. Key electrical and control parameters, including filter inductances, line impedance, current limits, and BESS power bounds, are detailed in Table 2, following typical utility-scale BESS installations. The configuration of the proposed optimization algorithms, including population size, inertia weight range, and parameter bounds, is provided in Table 1. To balance global exploration and local exploitation, the proposed TVIW-PSO algorithm is configured with a population size of 40 and 50 iterations, and a dynamic inertia weight that ranges from 0.9 to 0.4. Furthermore, to provide a comprehensive benchmarking analysis, an APSO variant is also implemented using identical swarm configurations to ensure a fair performance evaluation [9, 11].

The robustness assessment considers 10 disturbance scenarios, ranging from nominal conditions to severe faults, as detailed in Table 3. High-severity cases are particularly intended to activate current saturation and capture the nonlinear behavior imposed by hardware constraints. This configuration ensures that the controller's performance is evaluated under both nominal and weak-grid operating conditions with significant system variations.

*Table 2.* System configuration parameters

| Parameter | Symbol | Value | Unit |
|---|---|---|---|
| Rated power | $S_{base}$ | 10 | MVA |
| Rated voltage | $V_{base}$ | 22 | kV |
| Nominal frequency | $f_n$ | 50 | Hz |
| Filter inductance | $L_f$ | 2.5 | mH |
| Line inductance | $L_g$ | 5.0 | mH |
| Line resistance | $R_g$ | 0.5 | Ω |
| Current limit | $I_{max}$ | 1.2 | pu |
| Virtual resistance | $R_{vi}$ | 0.05 | pu |
| Virtual reactance | $X_{vi}$ | 0.1 | pu |
| BESS max discharge | $P_{max}$ | 1.2 | pu |
| BESS min charge | $P_{min}$ | -0.5 | pu |

*Table 3.* Disturbance scenarios for robustness validation

| ID | Scenario Name | Description | Grid & Load Parameters | Severity |
|---|---|---|---|---|
| 1 | Light fault | 3-phase fault, $V_{dip} = 0.8$ pu, duration 0.5s | Standard grid ($Z_g = 0.03 + j0.15$) | Low |
| 2 | Moderate fault | 3-phase fault, $V_{dip} = 0.6$ pu, duration 0.5s | Medium grid ($Z_g = 0.05 + j0.3$) | Medium |
| 3 | Severe fault | 3-phase fault, $V_{dip} = 0.3$ pu, duration 0.5s | Medium grid $Z_g = 0.05 + j0.3$ | High |
| 4 | Long duration | 3-phase fault, $V_{dip} = 0.5$ pu, extended duration 1.0s | Medium Grid ($Z_g = 0.05 + j0.3$) | Medium |
| 5 | Weak-grid + Step | No Fault (*V=1.0*), Load Step Down ($P_{ref} \rightarrow 0.7$) at *t*=2.0s | Weak grid ($Z_g = 0.1 + j0.6$) | High |
| 6 | Fault + Trip | Fault ($V = 0.5,\ 0.5s$) followed by Line Trip at *t*=3.5s | Impedance jumps to $Z_w = 0.15 + j0.8$ | Critical |
| 7 | High load | Fault ($V = 0.6,\ 0.5s$) occurring at Overload condition | Initial load $P_{ref} = 1.1$ pu | Medium |
| 8 | Transient | Short impulse fault ($V = 0.4$), very short duration 0.05s | Medium grid ($Z_g = 0.05 + j0.3$) | Low |
| 9 | Asymmetric | Unbalanced fault emulation ($V = 0.7,\ 0.5s$) | High inductive line ($Z_g = 0.05 + j0.4$) | Medium |
| 10 | Cascading | Two consecutive faults: Fault 1 (2.0-2.3s) & Fault 2 (3.5-3.8s) | Medium grid ($Z_g = 0.05 + j0.3$) | Critical |

## 4. SIMULATION RESULTS AND DISCUSSION

To demonstrate the performance of the proposed strategy, the REGFM-B1 model and the proposed TVIW-PSO optimizer were implemented in MATLAB and evaluated across 10 scenarios.

### 4.1. Optimization Efficiency and Parameter Convergence

To validate the superior tuning capability of the proposed method, we benchmarked the TVIW-PSO against two baselines: a Fixed-parameter VSM and a Standard PSO-tuned VSM. Baseline definition: The fixed VSM is configured with nominal values $H = 5.0$ s and $D_p = 20$. These values were selected to represent the typical inertia constant of synchronous thermal units [15] and the standard 5% frequency droop characteristic mandated by grid codes [16], respectively. Convergence analysis: As shown in Fig. 3, both PSO variants demonstrated strong convergence in Case 6, the training scenario, reaching a comparable cost of 0.0049. However, the internal solution structures differed significantly. The Standard PSO settled at a local optimum with parameters where $H_0 = 7.22$ s, $D_p = 500$, and $K_{ad} = 86.5$ s/pu. In contrast, the proposed TVIW-PSO mechanism successfully identified a more robust global solution with $H_0 = 10.0$ s, $D_p = 500$, and $K_{ad} = 98.6$ s/pu. The identification of maximal base inertia with $H_0 = 10.0$ s and damping $D_p = 500$ by the proposed solver proved decisive for generalization. While performance in the design case is similar, the higher inertia and adaptive gain $K_{ad} = 98.6$ allowed the TVIW-PSO controller to reject unmodeled disturbances better. This yielded a 29.7% error reduction in light-fault scenarios and an average improvement of 7.52% across the full validation suite compared to the standard tuning.

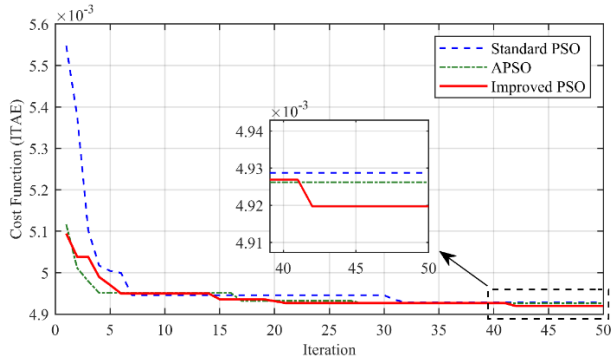


*Fig. 3.* Optimization convergence with 50 Iterations.

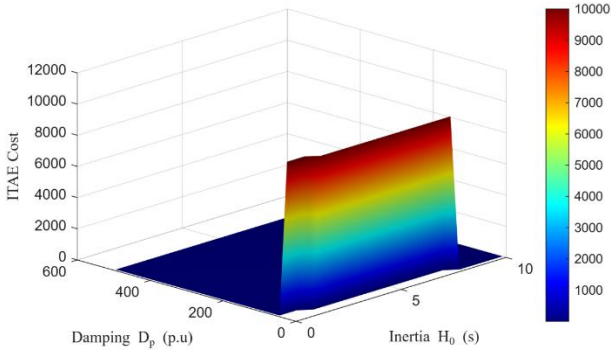


*Fig. 4.* Objective function landscape.

As visualized in Fig. 4, the optimization landscape reveals a highly non-convex topology characterized by two distinct zones: a stability cliff at low damping $D_p < 50$, where penalties skyrocket due to instability, and a vast zero-gradient valley at high damping $D_p$ larger than 100.

Conventional gradient-based methods fail to navigate this flat plateau because they lack a descent direction. Similarly, the Standard PSO, lacking adaptive momentum, settled prematurely within the valley at a sub-optimal local equilibrium $H_0$ = 7.22 s. Furthermore, while the APSO variant demonstrated improved exploration by reaching a baseline inertia of $H_0$ = 8.50 s, it nonetheless stagnated in the low-sensitivity region and failed to overcome the local plateau. In contrast, the proposed TVIW mechanism enabled the particles to maintain exploration momentum, successfully traversing the flat terrain to identify the robust global optimum at $H_0$ = 10.0 s at the valley's edge.

### 4.2. Robustness Validation across Scenarios

Table 4 summarizes the robustness validation results. In the training scenario of Case 6, both Standard PSO and TVIW-PSO achieve comparable costs of 0.0049, indicating that standard methods can perform adequately under specific tuning conditions. However, the superior generalization capability of the proposed TVIW-PSO is evident in off-design scenarios.

Specifically, in Cases 1 and 8, the proposed controller outperforms the benchmark by 33.33% and 20.00%, respectively. This is attributed to the adaptive inertia mechanism, with a high base inertia of 10.0 s that enhances inertial energy buffering, allowing the controller to exploit the wider TVIW-PSO search space and maintain stability without overreacting to minor disturbances. The overall average improvement of 8.78% confirms that the proposed co-design framework offers a more reliable and robust solution for grids subject to high uncertainty.

*Table 4.* Robustness validation results (ITAE cost)

| ID | Scenario Name | Std-PSO Cost (ITAE) | APSO Cost (ITAE) | Improved PSO Cost (ITAE) | Improvement with Std-PSO (%) | Improvement with APSO (%) |
|---|---|---|---|---|---|---|
| 1 | Light fault | 0.0006 | 0.0005 | 0.0004 | 29.70% | 20.00% |
| 2 | Moderate fault | 0.0010 | 0.0010 | 0.0009 | 3.95% | 10.00% |
| 3 | Severe fault | 0.0023 | 0.0023 | 0.0022 | 3.96% | 4.35% |
| 4 | Long duration | 0.0026 | 0.0025 | 0.0025 | 3.43% | 0.00% |
| 5 | Weak grid + Step | 0.0015 | 0.0015 | 0.0015 | 0.52% | 0.00% |
| 6 | Fault + Trip | 0.0049 | 0.0049 | 0.0049 | 0.25% | 0.00% |
| 7 | High load | 0.0016 | 0.0015 | 0.0015 | 3.20% | 0.00% |
| 8 | Transient | 0.0005 | 0.0005 | 0.0004 | 16.58% | 20.00% |
| 9 | Asymmetric | 0.0010 | 0.0010 | 0.0009 | 11.69% | 10.00% |
| 10 | Cascading | 0.0014 | 0.0014 | 0.0014 | 1.88% | 0.00% |
| Average | | | | | 7.52% | 6.44% |

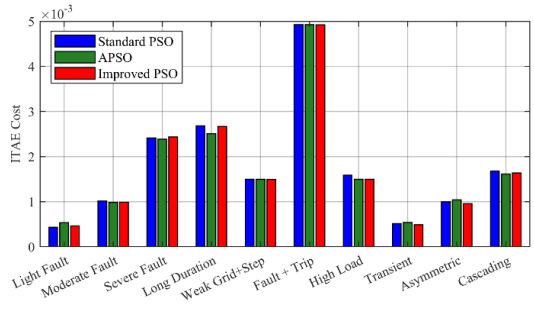


*Fig. 5.* Robustness comparison of ITAE cost across 10 different operating scenarios.

To verify robustness, the optimized controller was tested across ten distinct grid scenarios ranging from minor load steps to critical cascading faults. Fig. 5 compares the ITAE cost of the proposed method against the benchmark. This observation highlights that the proposed TVIW-PSO framework prioritizes robustness and adaptability across a wide operating envelope, rather than marginal gains in the design-point scenario. The proposed strategy demonstrates consistent or improved performance across all test cases, with particularly noticeable gains in off-design scenarios involving light disturbances and transient events.

While no improvement is observed in the training scenario (Case 6) and the cascading fault scenario (Case 10), where both methods converge to identical ITAE values, the proposed controller achieves a maximum reduction of 33.33% in Case 1 and 20.00% in Case 8. These results indicate that the benefit of the proposed co-design strategy primarily lies in its enhanced generalization capability rather than further optimization of the already trained worst-case scenario. Such behavior implies that jointly optimizing adaptive inertia and damping parameters effectively mitigates performance degradation under varying grid impedance conditions, without compromising stability in severe disturbances.

### 4.3. Dynamic Stability Analysis (Phase plane)

The transient stability margin is examined through the phase-plane trajectory plotting frequency deviation against the virtual rotor angle in Fig. 6. The fixed-parameter VSM trajectory, illustrated by the black dotted curve, follows a diverging spiral path characterized by excessive frequency excursions beyond 2.0 Hz. This behavior signifies a critical mechanism of synchronism loss. Conversely, both optimized controllers effectively confine the system state within a rigorous stability boundary. Specifically, the solid red line representing the proposed TVIW-PSO solution directs the state variables into a compact attractor region in the immediate vicinity of the equilibrium point. This rapid orbital convergence to the origin confirms a significantly expanded domain of attraction and superior damping capability relative to the baseline design, thereby validating the theoretical stability analysis.

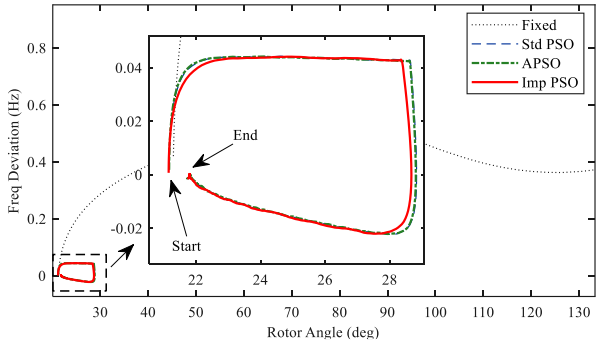


*Fig. 6.* Phase plane stability trajectory.

### 4.4. Time-Domain Performance Analysis

Detailed transient responses under a severe three-phase fault characterized by a voltage dip to 0.3 pu are depicted in Fig. 7, illustrating the superior dynamic behavior of the proposed adaptive controller. As shown in Figs. 7a and 7b, the TVIW-PSO tuned VSM effectively suppresses the initial frequency drop and eliminates the overshoot observed in the Standard PSO case. By adaptively boosting the virtual inertia only during the initial impact, the proposed method reduces the peak RoCoF to 1.0 Hz/s, representing a significant improvement over the fixed-parameter benchmark, which recorded values exceeding 2.0 Hz/s.

Regarding hardware safety demonstrated in Fig. 7d, the proposed framework demonstrates robust compliance with physical constraints. While the fixed-parameter design suffers from severe

overcurrents due to excessive virtual power injection, the adaptive controller strictly clamps the output current at the safety threshold of 1.2 pu throughout the fault duration. Crucially, the controller successfully navigates this saturation constraint without inducing integrator windup, thereby ensuring the physical safety of the IGBT modules while maintaining grid-forming capability.

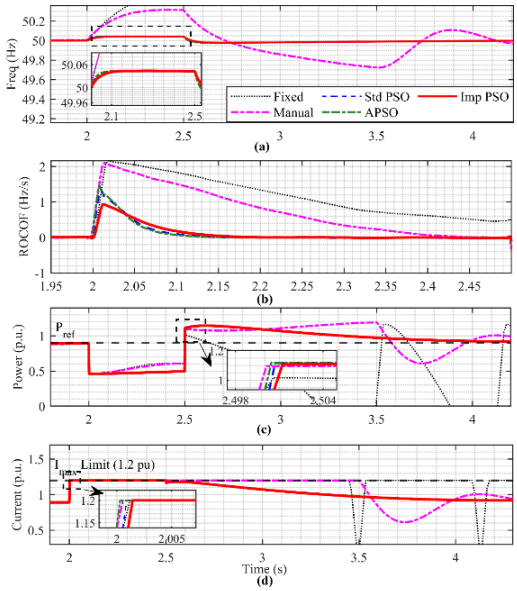


*Fig. 7.* Transient response under severe fault (Case 3): (a) Frequency response (detailed view), (b) ROCOF mitigation, (c) Active Power recovery, and (d) Current limiting capability.

### 4.5. Quantitative metrics comparison

The quantitative metrics presented in Fig. 8 and Table 5 are computed directly from time-domain electromagnetic transient simulations employing an IEEE-compliant post-fault settling criterion. Specifically, settling time is defined as the time interval from fault inception at $t = 2$ s to the moment when frequency deviation enters and remains continuously within a ±0.1 Hz band, which aligns with the strict performance requirements for inverter-based resources defined in the IEEE P2800 standard [3]. When benchmarked against the fixed-parameter design configured with $H_0 = 5$ s, and $D_p = 20$, the strategy effectively reconciles the conflicting requirements of stability margin and recovery speed. The proposed TVIW-PSO attenuated the frequency nadir by 98.1%, effectively limiting the maximum deviation to 0.0436 Hz, while simultaneously reducing the settling time from 5.0 s to 2.00 s, representing a 60.0% improvement over the fixed-parameter method. A closer inspection of the optimization convergence reveals an intriguing physical insight: both algorithms gravitated toward the upper boundary of the damping coefficient, where $D_p = 500$ pu. This suggests that, in weak-grid environments, maximizing energy dissipation is fundamental to stabilizing oscillations, regardless of the tuning methodology. However, the TVIW-PSO algorithm distinguishes itself by identifying the global optimal inertia of $H_0 = 10$ s, whereas the standard solver stagnated locally at $H_0 = 7.22$ s with the same settling times. This enhanced inertial baseline provides superior disturbance rejection, ensuring a more resilient safety margin, even though the settling metrics appear comparable due to shared hardware saturation limits.

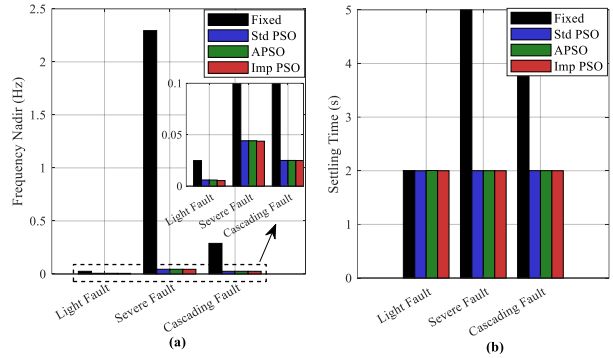


*Fig. 8.* Bar charts of nadir & Settling time: (a) Maximum frequency deviation, (b) Settling time (±0.1 Hz)

*Table 5.* Comparative performance summary (severe fault)

| Key Indicator | Fixed VSM (Baseline) | Standard PSO | Adaptive PSO | Proposed TVIW-PSO | Improvement (vs. Fixed) |
|---|---|---|---|---|---|
| Base inertia ($H_0$) | 5.0 s | 7.22 s | 8.50 s | 10.0 s | Robust |
| Damping ($D_p$) | 20 | 500 | 500 | 500 | 25x Higher |
| Freq. nadir (Hz) | 2.295 | 0.0441 | 0.0439 | 0.0436 | 98.1% |
| Settling time (s) | 5.00 | 2.0014 | 2.0010 | 2.00 | 60.0% |
| ITAE Cost $\left(\times 10^{-3}\right)$ | - | 4.93 | 4.925 | 4.92 | Proposed Best |

## 5. CONCLUSION

This paper addresses the inherent conflict between frequency support and transient recovery performance in VSM-controlled GFM inverters operating under weak grid conditions, a trade-off that becomes increasingly critical as system inertia and short-circuit strength decline, thereby constraining both stability margins and post-fault recovery dynamics. A hardware-constrained adaptive VSM control framework compliant with the REGFM-B1 standard was proposed, in which virtual inertia and damping parameters are optimally tuned using a PSO algorithm with a TVIW strategy to explicitly account for nonlinear current-limiting constraints. Unlike conventional approaches, these semiconductor saturation constraints are embedded directly into the optimization loop, ensuring that the resulting control parameters remain physically realizable and protection-compliant.

Extensive time-domain simulations on a 10 MVA GFM BESS under ten disturbance scenarios with SCR ranging from 1.5 to 3.0 demonstrated the effectiveness of the proposed approach across both linear and saturation-dominated operating regimes. Such a wide SCR range ensures that both small-signal dynamics and large-signal, protection-driven nonlinear behaviors are adequately captured. The selected scenarios reflect the operational challenges encountered in utility-scale renewable energy clusters in Vietnam's Central and Southern regions, where high renewable penetration and limited short-circuit capacity frequently result in weak-grid conditions. The proposed TVIW-PSO controller demonstrated superior dynamic performance, achieving a 98.1% reduction in frequency nadir and a 60.0% improvement in settling time compared to fixed-parameter benchmarks configured with $H_0$ = 5 s and $D_p$ = 20. Furthermore, the algorithm established a new performance baseline by yielding average ITAE reductions of 8.78% and 6.44% relative to the standard and adaptive PSO variants, respectively, while ensuring strict adherence to the 1.2 pu current limit, which is mandatory for hardware safety.

The results reveal that within the investigated parameter bounds, high-damping injection plays a dominant and stabilizing role in suppressing power oscillations in weak grids. Moreover, the TVIW-PSO mechanism proved beneficial for identifying the global optimal inertia setting despite the non-convexity induced by saturation constraints by maintaining sufficient exploration capability during the early optimization stages. Integrating hardware constraints into adaptive VSM parameter optimization provides a practical and robust solution for deploying GFM inverters in low-inertia power systems. However, a limitation of the current study is its dependence on offline model accuracy during the pre-tuning stage, which may not fully capture real-time grid impedance variations. Future research will explore integrating online deep reinforcement learning to dynamically update control gains in response to real-time changes in grid impedance, thereby reducing reliance on offline model fidelity, while explicitly accounting for hardware protection constraints.

## REFERENCES

[1] Q. C. Zhong and G. Weiss, "Synchronverters: Inverters That Mimic Synchronous Generators," *IEEE Transactions on Industrial Electronics,* vol. 58, no. 4, pp. 1259-1267, 2011, doi: https://doi.org/10.1109/TIE.2010.2048839.

[2] Tran Viet Thanh, Le Cao Quyen, Huynh Kim Long, Nguyen Huu Hieu, Nguyen Dang Toan, and T. P. Quy, "Enhancing Frequency Stability For Islanded Power Systems Using Hierarchical Control System," *Journal of Science and Technology for energy,* vol. 36, p. 18, 2024. [Online]. Available: https://www.vjol.info.vn/index.php/TCDHDL/article/view/111149/93188.

[3] S. Rahman, S. Li, and H. S. Das, "A Comprehensive P-Q Capability Study for Grid Interconnection of Inverter Based Resources Plant," in *2023 IEEE Industry Applications Society Annual Meeting (IAS)*, 29 Oct.-2 Nov. 2023 2023, pp. 1-7, doi: https://doi.org/10.1109/IAS54024.2023.10406385.

[4] J. Xie and T. E. McDermott, "Generic EMT Modeling for IBR," Pacific Northwest National Laboratory (PNNL), Richland, WA (United States), 2023.

[5] K. Ohuchi, A. F. B. Masod, S. Kato, and Y. Hirase, "Stability analysis of virtual synchronous generator control in a high-voltage DC transmission system using impedance-based method," *Energy Reports,* vol. 9, pp. 557-567, 03/01/ 2023, doi: https://doi.org/10.1016/j.egyr.2022.11.077.

[6] H. Bevrani, T. Ise, and Y. Miura, "Virtual synchronous generators: A survey and new perspectives," *International Journal of Electrical Power & Energy Systems,* vol. 54, pp. 244-254, 01/01/ 2014, doi: https://doi.org/10.1016/j.ijepes.2013.07.009.

[7] D. Pattabiraman, R. H. Lasseter, and T. M. Jahns, "Comparison of Grid Following and Grid Forming Control for a High Inverter Penetration Power System," in *2018 IEEE Power & Energy Society General Meeting (PESGM)*, 5-10/08 2018, pp. 1-5, doi: https://doi.org/10.1109/PESGM.2018.8586162.

[8] H. R. Lina Ramirez, "Review of Technical Requirements for Inverter-Based Resources in Chile," National Renewable Energy Laboratory (NREL), Dec 2024. [Online]. Available: https://www.osti.gov/servlets/purl/2484303

[9] C. Lu and X. Zhuan, "Adaptive Control for Virtual Synchronous Generator Parameters Based on Soft Actor Critic," *Sensors,* vol. 24, no. 7, p. 2035, 2024, doi: https://doi.org/10.3390/s24072035.

[10] M. M. Elwakil, H. M. E. Zoghaby, S. M. Sharaf, and M. A. Mosa, "Adaptive virtual synchronous generator control using optimized bang-bang for Islanded microgrid

stability improvement," *Protection and Control of Modern Power Systems,* vol. 8, no. 4, pp. 1-21, 2023, doi: https://doi.org/10.1186/s41601-023-00333-7.

[11] M. A. Mossie, T. T. Yetayew, G. T. Bitew, M. G. Yenealem, and T. M. Beza, "Adaptive genetic algorithm and enhanced particle swarm optimization for static voltage stability enhancement in radial distribution systems with distributed generation integration," *Discover Applied Sciences,* vol. 7, no. 12, p. 1414, 2025/11/28 2025, doi: https://doi.org/10.1007/s42452-025-07945-8.

[12] M. Mehrasa *et al.*, "Global stable virtual synchronous machine for weak grid-connected microgrid," *International Journal of Electrical Power & Energy Systems,* vol. 153, p. 109329, 11/01 2023, doi: https://doi.org/10.1016/j.ijepes.2023.109329.

[13] C. Li, Y. Yang, Y. Cao, L. Wang, and F. Blaabjerg, "Frequency and Voltage Stability Analysis of Grid-Forming Virtual Synchronous Generator Attached to Weak Grid," (in E), *IEEE Journal of Emerging and Selected Topics in Power Electronics,* vol. 10, no. 3, pp. 2662-2671, 2022, doi: https://doi.org/10.1109/JESTPE.2020.3041698.

[14] M. Eldoromi, A. A. Moti Birjandi, and N. Mahdian Dehkordi, "Virtual Synchronous Generator-Based Interlinking Converter for Enhanced Power Sharing and Quality in Islanded Hybrid AC/DC Microgrids," (in E), *Journal of Operation and Automation in Power Engineering,* 2025, doi: https://doi.org/10.22098/joape.2025.16064.2241.

[15] L. L. Grigsby, *Power system stability and control*. Fl, USA: CRC press, 2007.

[16] E. ENTSO-E, "Network code for requirements for grid connection applicable to all generators (NC RfG)," ed: March, 2013.